



## Real-time internal temperature estimation of commercial Li-ion batteries using online impedance measurements

Kieran Mc Carthy <sup>a</sup>, Hemtej Gullapalli <sup>b</sup>, Tadhg Kennedy <sup>a,\*</sup>

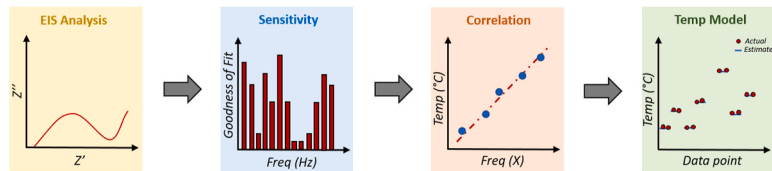
<sup>a</sup> Bernal Institute and Department of Chemical Sciences, University of Limerick, Limerick, V94 T9PX, Ireland

<sup>b</sup> Analog Devices, 125 Summer St, MA, 02110, Boston, United States

### HIGHLIGHTS

- Impedance-temperature relationship allows for estimation of battery temperature.
- Online acquisition of impedance while the battery is under load.
- High internal temperature estimation accuracy over extended cycles.
- Calibration of impedance to the change in temperature.

### GRAPHICAL ABSTRACT



### ARTICLE INFO

#### Keywords:

Electrochemical impedance spectroscopy  
Temperature  
Li-ion

### ABSTRACT

Thermal monitoring of Li-ion batteries, particularly when a large number of batteries are interconnected, is a mandatory requirement to ensure their safety, performance and longevity. In this paper, a real-time internal temperature estimator for Li-ion polymer batteries is introduced. Firstly, the influence of temperature on the impedance characteristics of the battery at various frequencies was explored. Next, the influence of state of charge (SoC) and state of health (SoH) on the different parts of impedance were examined. The insights learned were used to develop a temperature estimation model based on a single-point frequency measurement at 200 Hz. All impedance measurements were performed online while the cell was under load. The impedance at 200 Hz demonstrated high sensitivity to changes in temperature and low sensitivity to SoC and SoH. The model was validated experimentally using data collected from 9 separate cells cycled over 100 times each. The average RMSE of the estimated temperature across all data sets was 1.41 °C, confirming the accuracy of the model.

### 1. Introduction

The ever-increasing adoption of Li-ion batteries (LIB) in automotive and grid-energy storage applications has increased demand for higher capacity LIBs and a new requirement for faster charging to satisfy customer demand. The internal temperature (IT) of a LIB, which cannot be directly measured using current approaches, must be estimated to ensure a LIB operates within predefined temperature limits. The IT of a LIB can quickly rise when it is subjected to large amounts of current, with differences of as much as 10 °C developing between the battery

core and surface [1,2]. The narrow temperature operating window for LIBs (0 – 40 °C for charge and -10 - 55 °C for discharge) means an accurate thermal management system is required to ensure safe operation [3]. Excessively high temperatures can result in a thermal runaway and the venting of toxic gases while low temperatures can lead to a short-circuit [4]. While the occurrence of these incidents is rare, poor management of LIB temperature can result in large-scale recalls of cells and endangerment to human life.

Existing temperature monitoring approaches typically use surface mounted temperature sensors located on the battery with a thermo-

\* Corresponding author.

E-mail address: [Tadhg.kennedy@ul.ie](mailto:Tadhg.kennedy@ul.ie) (T. Kennedy).

electric model capable of estimating the internal cell temperature [5]. The use of surface mounted temperature sensors has drawbacks, as in some instances they cannot detect rapidly rising temperatures sufficiently fast enough due to time taken for the heat to propagate from the core to the surface [6]. Electric vehicles typically contain hundreds of cells in series and parallel connections and so it is deemed too expensive to have a surface temperature sensor for each cell. As such, one sensor is used to acquire the temperature of a module as opposed to an individual cell [7]. An example of this is with the Chevrolet Volt and the Toyota Prius that use 16 and 42 temperature sensors respectively to manage 288 cells [8].

Despite their limitations, the use of surface temperature and electrochemical models is the most commonly used commercial method of estimating internal temperature. The Kalman filter, used for tracking and predicting changes in a state, is often used with these models to estimate internal temperature with high accuracy [2,9–11]. Thermal models can achieve accurate predictions of internal battery temperature, however, are often computationally intensive and hard to implement on small devices with limited memory, such as mobile phones. These models require extensive information on the battery's properties in order to be effective. A battery is made from multiple layers of anode, separator, cathode, current collector and electrolyte, often tightly wound together, and so modelling the interaction of each during operation is challenging [12]. The internal resistance of the battery is often required in these models, but is difficult to estimate accurately using current approaches, as it changes based on the state of charge (SoC), state of health (SoH) and temperature of the battery.

An alternate approach to internal temperature estimation is the use of electrochemical impedance spectroscopy (EIS) to ascertain the impedance at a single or wide range of frequencies to gain real-time knowledge of the effect of temperature on the inner processes of a battery [13–17]. EIS is a non-destructive and non-invasive technique that can monitor parameters such as internal resistance, charge transfer resistance, double-layer capacitance and diffusion [18,19]. 'Sensorless' is often used to describe EIS as a temperature estimation tool as it requires no other forms of hardware. Another advantage of using EIS is the avoidance of the heat transfer delay conundrum that is seen when using surface temperature sensors. An intrinsic relationship exists between battery impedances at certain frequencies and battery IT, however this relationship is also influenced by parameters such as battery SoC and SoH. Existing work by Srinivasan [13,14,20], Schmidt [15,21,22] and others [11,17,23–26] have confirmed relationships between certain frequencies and internal battery temperature. Srinivasan demonstrated that for LiCoO<sub>2</sub> LIBs, frequencies between 40 and 100 Hz are highly sensitive to changes in temperature while also being insensitive to changes in SoC and SoH [13]. The majority of existing approaches use offline EIS measurements to update their models. Advancements in the miniaturising of EIS capable devices mean it is now possible to include it as a monitoring device on BMS's. Panasonic has recently developed an EIS chip that can accurately measure the impedance of multi-cell stacked LIBs [27]. This device was capable of achieving accurate impedance data on par with standard benchtop equipment. Analog Devices Inc. have also developed a chip-scale EIS device (AD594X) for battery applications. This device can accurately measure impedances in the milliohm range and includes all circuitry required to create and measure excitation signals over a wide range of frequencies [28].

In this study, an internal temperature estimation model is proposed using the impedance gathered at a single frequency, which allows for near instantaneous acquisition of battery internal temperature. All results in this paper are based on online EIS measurements (i.e. while the battery is under load), which validates its use as a potential temperature estimator in real-world applications. Firstly, the intrinsic relationship between certain frequencies and IT was explored. Secondly, the effect of SoC and SoH on the temperature estimates were studied. Accordingly, an internal temperature estimation model was developed to account for the influence of each parameter on the temperature estimate. Multiple

batteries were tested using random changes in temperature and over extended cycles (100 cycles), which validates the high reliability and accuracy of the proposed model. To our knowledge, this is the first time temperature estimation via impedance has been demonstrated over extended cycling. These results demonstrate the potential of using EIS as an online temperature estimator.

## 2. Experimental

The flowchart in Fig. S1 illustrates the experimental test procedure. LCO Li-polymer batteries with a capacity of 2.8 Ah and a nominal voltage of 3.7 V were used for all experimentation. The battery test bench consisted of an Arbin Battery Cycler (5 V, 5 A) consisting of 48 channels, a Gamry Interface 5000P multiplexed across all channels, a MZTC Arbin climate-controlled chamber (with an adjustable range of 10 °C–60 °C) and a computer for control and analysis. All tests were performed inside the climate-controlled chamber to ensure a constant temperature was obtained. For each change in temperature the battery was acclimatized for 60 min at OCV to ensure the cells IT was the same as the environmental chamber before cycling commenced.

All batteries were charged at 25 °C using a constant current (CC) of 1 A from 3.20 V – 4.20 V followed by a constant voltage (CV) step at 4.20 V until the applied current had declined to 0.15 A. The chamber temperature was altered from 10 °C to 55 °C only during discharge. Temperature estimation only during the discharge stage of the battery was considered as the high variable discharge currents of an electric vehicle could potentially lead to less accurate temperature estimation and increased battery heating as opposed to the typical constant current applied during charging. High variable currents can cause rapid heating of the battery and so the potential for the batteries to heat above a maximum threshold was deemed to be higher. Additionally, as the batteries in an electric vehicle need to operate in a constantly changing environmental temperature, the need for accurate temperature estimation during discharge is potentially more vital. Galvanostatic EIS was performed using an AC amplitude RMS of 0.010 A during discharge every 10 min. This amounted to a total of ~32 EIS scans between the frequency range of 1 Hz–10 kHz. A DC bias equal to the discharge current (0.50 A) was used so the cell continued to discharge while the EIS scan took place. Testing was stopped after 100 charge/discharge cycles had been completed. A comparison of the EIS test conditions used in this paper with existing studies can be found in Table S1.

### 2.1. Theory of electrochemical impedance spectroscopy

EIS is a powerful characterisation technique that can be used to gain in-depth insights into the electrochemical behaviour of a battery. It allows many different internal processes, such as the ohmic resistance, charge-transfer resistance, double-layer capacitance and diffusion properties of a battery to be monitored [29]. Each aforementioned process has a different time constant, which can be examined by adjusting the applied AC frequency over a wide range. In practice, a sinusoidal signal is injected into the battery at a particular frequency and the response signal, which changes depending on the impedance of the battery, is analysed. The applied signal can be a voltage or a current, although galvanostatic EIS is typically used for LIBs. The impedance can then be calculated using the following equation:

$$Z = \frac{V_t}{I_t} = \frac{\hat{V}\sin(\omega t)}{\hat{I}\sin(\omega t + \phi)} = Z_0 \frac{\sin(\omega t)}{\sin(\omega t + \phi)} \quad (1)$$

Where  $V_t$  and  $I_t$  are the potential and current at time  $t$ ,  $\hat{V}$  and  $\hat{I}$  are the amplitudes of the voltage and current signals,  $\phi$  is the phase shift and  $Z_0$  is the magnitude of impedance. The impedance can then be expressed as a complex number comprised of both real ( $Z'$ ) and imaginary ( $Z''$ ) values using the following equations:

$$Z' = Z_o \cos(\phi) \quad (2)$$

$$Z'' = Z_o \sin(\phi) \quad (3)$$

$$Z_o = \sqrt{Z'^2 + Z''^2} \quad (4)$$

The phase angle can be determined from the imaginary and real impedance values using the following equation:

$$\tan(\phi) = \frac{Z''}{Z'} \quad (5)$$

## 2.2. Model parameter fitting

In order to quantify the change in impedance to the change in temperature, online EIS was performed at temperatures ranging from 10 °C to 55 °C in 5 °C increments during the entirety of the discharge step [100% SoC – 0% SoC]. This was performed so the effect of SoC on the temperature estimate could also be ascertained. The average impedance value at each frequency across the entirety of the discharge step was calculated and used for model parameter fitting. Surface thermocouples placed on the battery verified that a discharge current of 0.50 A did not cause internal heating and an acclimatization step of 60 min was sufficient to ensure the surface battery temperature was the same as the chamber temperature. As the internal battery temperature cannot be directly measured, stable surface temperature readings over a 60 min period were used to infer the average temperature of the whole battery. Linear regression was used to relate the  $y$  variable, the imaginary part of impedance at 200 Hz, to the  $x$  variable, temperature (Equation (6)). A calibration step was performed for each individual battery.

$$y = \alpha + \beta x \quad (6)$$

Eq. (6). Linear fit equation where  $y$  is the imaginary impedance value acquired at 200 Hz,  $\beta$  is the slope,  $\alpha$  is the  $y$  – intercept and  $x$  is the temperature estimate.

Two linear fits from 10 °C to 35 °C and 35 °C to 55 °C were required to accurately fit the experimental results. Once the imaginary part of the impedance at 200 Hz passed a predefined impedance threshold, which was determined via the calibration and differed slightly for each battery, the model switched to the coefficients for temperatures above 35 °C. Model coefficients were adjusted, based on the calibration data, to acquire the most accurate temperature estimate. These coefficients were then used for the subsequent 100 cycles. A periodic calibration could be performed in order to re-adjust the model for changes in the impedance-temperature relationship. As the ageing of a battery will invariably lead to an increase in its internal resistance, a periodic calibration would allow the model to adapt to changes in battery SoH. A single-point calibration at a known temperature could be employed using the temperature data from the thermistor located on the BMS in order to infer the internal temperature of the battery. The battery would need to be at rest for a sufficient period of time so the increase in temperature caused by the battery being under load could be mitigated. The relative change in impedance at this temperature, compared to the initial calibration, could then be measured and the model corrected. This calibration procedure would also allow the effects of a soft short to be accounted for and even detected. This is explained in detail in section 1 of the supporting information section. Temperature tests at 45 °C were not performed, due to limitations on the number of parameters that could be used in the experimental procedure.

## 3. Results

The premise of this study is to identify specific frequency's that are highly sensitive to changes in temperature while simultaneously being insensitive to the effects of SoC and SoH. From this analysis, a model was developed using the correlation between impedance and temperature to

estimate the average IT of the battery. A major advantage of this approach is the use of a single frequency point, in comparison to multiple frequencies, which can take a prolonged period of time to perform, thus the single frequency approach allows for near instantaneous gathering of data.

### 3.1. Effect of temperature on the electrochemical behaviour of the battery

In this section, the influence of temperature on the electrochemical behaviour of a LIB was examined. Typically, LIBs are designed to operate at their most efficient at room temperature (25 °C) with both lower and higher temperatures having a direct influence on a batteries performance. Fig. 1a compares the voltage discharge curves of a LIB as a function of temperature. It can be seen that a decrease in temperature was accompanied by a reduction in the potential window as well as the available capacity of the battery. This reduction in potential is caused by a decrease in electrolytic and solid electrolyte interface (SEI) conductivity, which in turn increases the polarization of the cell [23]. The internal resistance of a battery is not always constant and can vary greatly with temperature. As a battery is chemical in nature, the speed at which a reaction can occur is heavily influenced by temperature and follows the Arrhenius equation. Operating a battery at higher temperatures can increase the available capacity that can be extracted but shortens its lifespan [30]. Excessive heat can cause the decomposition of the electrolyte and formation of strong acids. Additionally, it can cause structural phase changes to the composition of the cathode and degrade the stability of the SEI layer [31]. The electrochemical performance of a LIB is reduced at low temperatures due to the increased internal resistance of the battery. Fig. 1b illustrates the discharge capacity as a function of temperature. The decrease in available capacity originates from the increase in the batteries charge-transfer resistance, which can be attributed to the decreased reaction kinetics at low temperatures [32]. Increasing the temperature improves electrolyte and SEI conductivity, thus increasing the available discharge capacity. At low temperatures, the electrolyte becomes more viscous which in turn reduces its ionic conductivity. Thus, a rise in the batteries internal resistance is observed due to the increased difficulty experienced by lithium ions when migrating to the electrodes [3].

EIS analysis of the behaviour of the LIB with changing temperature was performed to gain insights into the impedance-temperature relation. EIS was performed in 5 °C increments from 10 °C to 55 °C with the exception of 45 °C as the test procedure was limited to 9 different temperatures. The battery was charged at 25 °C and discharged at temperatures ranging from 10 °C to 55 °C. The battery was allowed to acclimatize for 1 h at the designated temperature before discharging. This was to ensure its internal temperature was the same as the temperature chamber. Fig. 2a shows the temperature dependency of the battery impedance from 10 °C to 55 °C, over the frequency range of 10 kHz – 1 Hz. Impedance spectra are presented in a Nyquist plot, which consists of a large semi-circle like shape and a line at an approximate 45° angle. It is presumed that the high frequency region is on the left and the low frequency region is on the right. By examining the impedance spectra on a Nyquist plot, information regarding the ohmic and charge-transfer resistance could be determined. It can be seen that the impedance increased as the temperature decreased with the opposite true for high temperatures. An equivalent circuit model (ECM) was used to interpret and analyse the impedance data at each temperature (Fig. S2). The ohmic resistance, which is the intersection of the spectra with the x-axis (only has ohmic contribution i.e. the imaginary part of impedance is equal to zero), remained relatively stable at each temperature whereas a large increase in charge-transfer resistance, which is the size of the semi-circle shape, was observed for low temperatures (Fig. 2b and 2c). At 10 °C the ohmic resistance of the LIB was 0.029 Ω. A linear decrease in ohmic resistance was observed as the temperature increased, with the LIB demonstrating a  $R_o$  value of 0.024 Ω at 55 °C. The charge-transfer resistance showed a much larger variation with temperature and

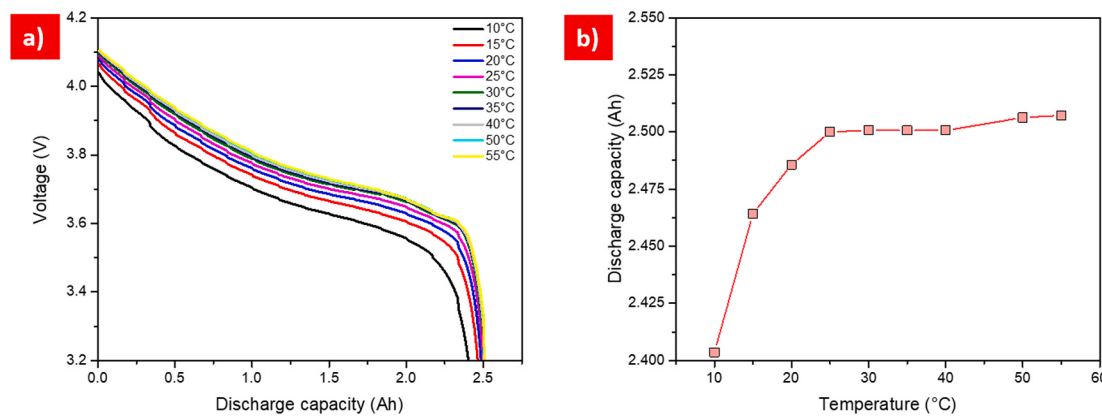


**Fig. 1.** a) Discharge – capacity plot of a Li-ion polymer battery at temperatures ranging from 10 °C to 55 °C. b) Discharge capacity as a function of battery temperature.

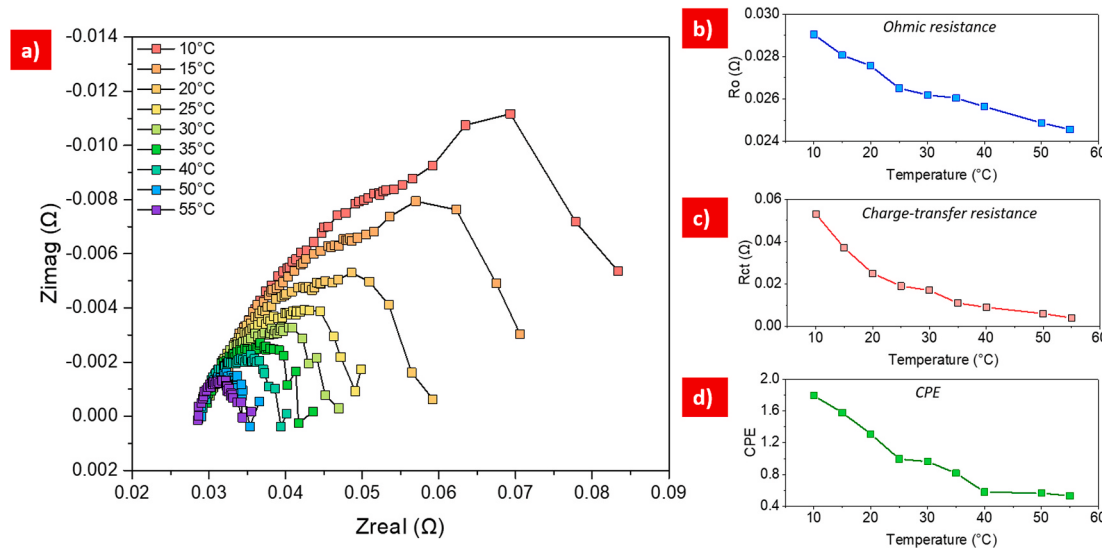


**Fig. 2.** a) Nyquist plot, b) ohmic resistance, c) charge-transfer resistance and d) CPE element as a function of temperature. EIS measurements were performed at 100% SoC.

demonstrated a 13.25x decrease in charge-transfer resistance from 10 °C to 55 °C. The CPE element in Fig. 2d also displayed an increase in magnitude as the temperature decreased. The variation in the cell impedance can be attributed to the increased/decreased kinetics of the cell at different temperatures. At low temperatures, the conductivity of the electrolyte and SEI is reduced [33], which leads to slow lithium diffusion between the anode and cathode [34,35] and an increase in resistance at the electrode surface [36–38]. At high temperatures, the diffusion and charge-transfer reaction processes are more efficient and so the battery impedance is lower [39]. Additional ECM analysis as a function of SoC and SoH can be found in supporting Fig. S3.

### 3.2. Identifying the optimal frequency for IT estimation

The impedance spectra at various SoCs, SoHs and temperatures were next examined in order to identify the optimal frequency to assess the IT with minimal interference from SoC and SoH. Fig. 3 examines the effect of SoC (3a-c), SoH (3d-f) and temperature (3g-i) on frequency. The phase and imaginary parts of impedance in Fig. 3a and 3b show minimal difference at each SoC from 10 kHz to 100 Hz. Frequencies under 100 Hz show an increase in phase and imaginary impedance as the SoC decreases. Likewise, the real part of impedance in Fig. 3c shows a similar trend at frequencies below 40 Hz with 0 % SoC showing a much larger

increase in impedance compared to all other SoCs. The charge-transfer resistance of the LIB increased as the SoC decreased, which caused the phase, imaginary and real parts of impedance to also increase (Fig. S5). Low frequencies, which are used to model the diffusion-controlled region, are highly dependent on SoC due to changes in the double-layer capacitance, current density and solid-state diffusivity at one or both electrodes [40,41]. These factors are dependent on the intercalated lithium content at each electrode. This increased sensitivity to SoC at low frequencies has previously been used to directly infer SoC [42–45].

EIS is well-known as a valuable tool for the prognostic and diagnostic analysis of battery ageing [46–49]. Fig. 3d, 3e and 3f explore the sensitivity of the phase, imaginary and real parts of impedance as a function of SoH. The battery underwent accelerated ageing using high currents until its measured capacity was only 80 % its initial. The change in the overall capacity resulted in large changes to the impedances. In Fig. 3d, we see an initial decrease in the magnitude of the phase part of impedance from 100 % to 95 % SoH. This is likely caused by the resistance of the battery decreasing as the active materials become fully activated and saturated with electrolyte. From 95 % to 80 % SoH, an increase in the magnitude of the impedance phase from 10 kHz to 10 Hz was observed. At frequencies lower than 10 Hz, noise interference affected the accuracy of the impedance measurement and so no discernible trend could be identified. The increase in phase impedance is

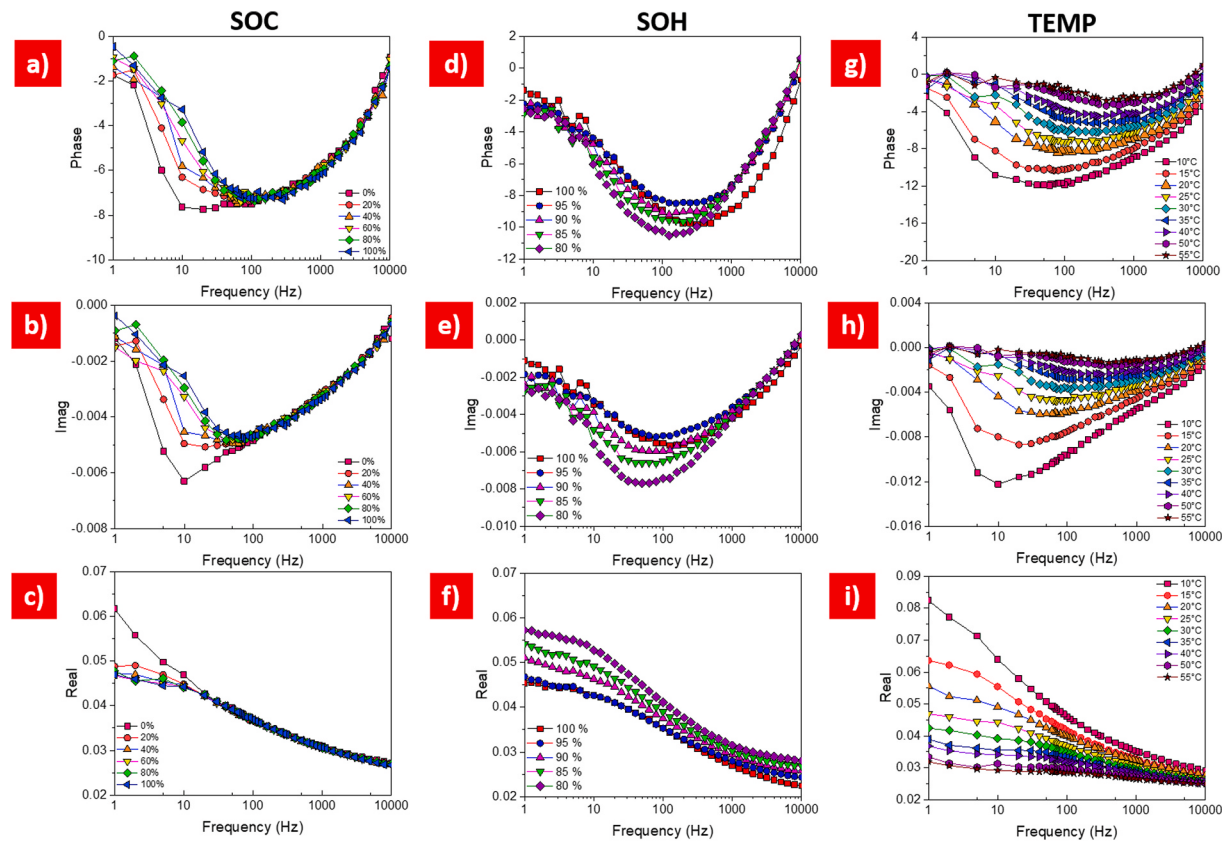


Fig. 3. Examines the effect of SoC (a-c), SoH (d-f) and temperature (g-i) on the phase, imaginary and real parts of impedance from 10 kHz–1 Hz.

most evident at the arc, or maximum phase, present at approximately 100 Hz. This is much more pronounced when we examine the imaginary part of impedance in Fig. 3e, where the impedance at 100 Hz increased from  $-0.0055$  to  $-0.0074$  for 100 % and 80 % SoH. Similarly, a decrease in the magnitude of the imaginary impedance was observed from 100 % to 95 % SoH. The real part of impedance showed the most linear increase in impedance as a function of SoH, increasing across all frequencies (Fig. 3f). The real part of impedance is used most frequently in literature to determine battery SoH, due to its dependence with SEI formation and electrolyte degradation, which are the electrochemical processes most influenced by ageing [50–52]. The increase in impedance as a battery ages is typically attributed to the increase in the electrodes charge-transfer resistances due to growth of the SEI [53]. Other age related processes that increase impedance include the active material not being electrically connected to the current collector [54]. The sensitivity of battery impedance with respect to temperature at certain frequencies was examined in Fig. 3g, 3h and 3i. An increase in impedance across all frequencies was observed with decreasing temperature

for phase, imaginary and real parts of impedance. Low temperatures affect the properties of the electrolyte, causing it to become more viscous, resulting in a reduction in its ionic conductivity [32]. The internal resistance subsequently rises due to the increase in the impedance of the migrating Li-ions. At high temperatures, the kinetics of the battery increase due to improved electrolyte conductivity causing a reduction in charge-transfer impedance [3]. A much larger difference in impedance was observed between 10 °C and 15 °C compared to all other temperatures.

Using the impedance data gathered at various SoCs, SoHs and temperatures, a frequency correlation analysis with each parameter was performed to identify the dependency each specific frequency and part of impedance had with the change in the aforementioned parameters. Fig. 4 examines the correlation or goodness of fit (GOF) that the imaginary, real and phase parts of impedances at particular frequencies have with the change in temperature, SoC and SoH. A GOF calculation determines how strong of a linear relationship there is between two variables. The impedances at particular frequencies were plotted against the

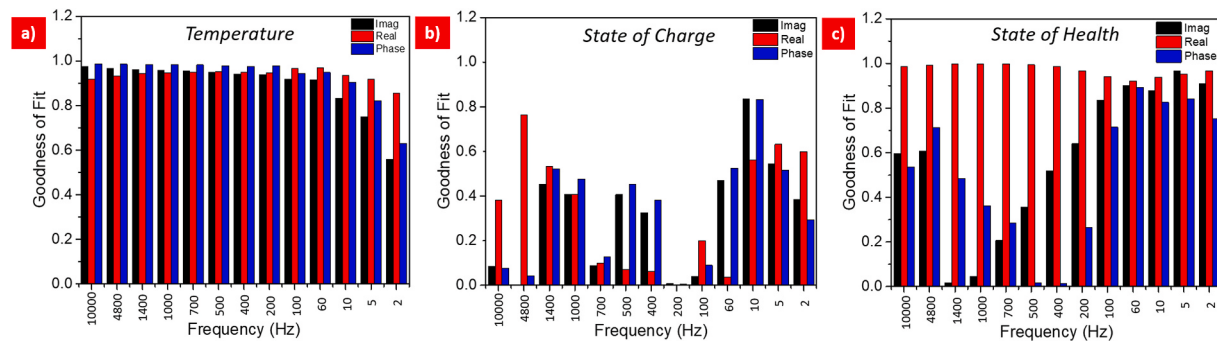


Fig. 4. Goodness of fit plots for the imaginary, real and phase parts of impedance at particular frequencies for a) temperature, b) SoC, and c) SoH.

change in temperature, SoC and SoH and the variability caused by the relationship with the other factor was determined. The closer the value is to 1 indicates the greater the relationship with the parameter being examined and is taken to be a highly reliable parameter to use for future model prediction, whereas a value close to 0 indicates the model parameter failed to accurately relate to the other parameter. As we have seen in the previous section, the imaginary, real and phase parts of impedance change with temperature (Fig. 4a). This change resulted in a GOF value close to 1 for the real, phase and imaginary parts of impedance from frequencies 10 kHz – 60 Hz with the exception of frequencies lower than 10 Hz, which had values ranging from 0.9 to 0.6. In Fig. 4b, the lower frequencies showed the greatest fit with SoC, particularly the imaginary and phase parts of impedance at 10 Hz (values of 0.8). The high correlation of lower frequencies with SoC explains the lower GOF values seen with frequencies 10 Hz – 2 Hz for temperature. Interestingly, all parts of impedance at 200 Hz showed little to no correlation with SoC, validating its suitability to be used for temperature estimation (Fig. S5).

The real part of impedance for each frequency in Fig. 4c showed the greatest fit with SoH at all frequencies with an average GOF value of 0.972 across all frequencies. Real impedances show high dependency to resistances from the SEI layer and electrolyte decomposition, two of the main causes of battery ageing. The imaginary part of impedance had the overall second best GOF values of all parts of impedance, particularly in the low-frequency region between 200 Hz and 2 Hz, with GOF values of 0.966 and 0.909 recorded for 5 Hz and 2 Hz. The lowest GOF value occurred at 1400 Hz (0.0162) at which point it increased linearly to 0.9006 at 60 Hz. Overall, the phase part of impedance showed the least correlation to SoH with an average GOF value of 0.515 across all frequencies. Similarly, the low frequency region of 100 Hz – 2 Hz presented the highest GOF values for the phase part of impedance. The lowest GOF values occurred at 500 Hz (0.0166) and 400 Hz (0.0141), with both higher and lower frequencies demonstrating much higher GOF values. The acquired impedances are a combination of both the anode and the cathode, which are highly dependent on the charge-transfer kinetics at each electrode. As each electrode in the battery is porous, the resistances and capacitances are distributional. Without the use of a three-electrode setup, it can be very difficult to isolate the individual impedances from the anode and cathode. The different lithiation states of each electrode have a direct influence on the porosity and conductivity of the active materials, and consequently the impedance at a particular time [55]. As such, choosing a frequency that is highly insensitive to SoC is of vital importance. Analysing these results in full, the impedance at 200 Hz was chosen as the impedance variable in the temperature model due to its low correlation with SoC and SoH and high dependence with the change in temperature. The real part of impedance was excluded due to its high correlation with the change in SoH. On further analysis of the phase and imaginary parts of impedance at 200 Hz, the imaginary part of impedance was selected, as the phase part of impedance is combined of both imaginary and real impedances and so was determined to be more sensitive to ageing related electrochemical processes. Examination of the GOF fitting graph for the phase and imaginary parts of impedance in Fig. S4 also highlights that although the imaginary part of impedance achieved a higher GOF value, a clear trend can be seen with the phase part of impedance to the change in SoH. This compares well with existing studies that show that the frequency range of 40 Hz – 400 Hz is associated with impedances from the SEI layer, and have been previously used for temperature estimation [13,15]. The SEI layer has previously been shown to be largely unaffected by changes in SoC as it is incapable of storing energy. Although the impedance is a combination of both electrodes, particular frequency ranges are highly dominated by either the anode or the cathode. The lower frequency range (<1 Hz) is dominated by the diffusion of Li<sup>+</sup> back and forth from the anode and cathode. In the middle frequency range of 1 Hz–10 Hz the impedance is dominated by the cathode and at high frequencies (>100 Hz) the impedance is dominated by the anode [56].

### 3.3. Fitting model parameters

To correlate the change in temperature to the imaginary part of impedance at 200 Hz, temperature tests were performed with online EIS measurements. This frequency was chosen based on analysis from the GOF plots in the previous section. Fig. 5 illustrates the linear fitting of the imaginary part of impedance at 200 Hz to temperature. Initial results using one linear fit across all temperatures (10 °C – 55 °C) produced an R<sup>2</sup> value of 0.9387 (Fig. 5a). Temperature estimation over 100 cycles was performed using this fit with the first 15 cycles shown in Fig. 5b. The measurement number refers to the amount of EIS scans that were performed. The resultant estimation yielded a large temperature RMSE of 12.49 °C over 100 cycles (Fig. 5b). Two linear fits from 10 °C to 35 °C and 35 °C to 55 °C were used to improve the linear fitting, as the imaginary part of impedance at 200 Hz did not show a perfect linear trend with temperature. This fitting yielded R<sup>2</sup> values of 0.9839 and 0.9909 for 10 °C to 35 °C and 35 °C to 55 °C respectively. The resultant estimation showed a marked improvement in accuracy with a temperature RMSE of 1.36 °C over 100 cycles.

The effect of SoC on the temperature estimate at each individual temperature for the imaginary part of impedance at 200 Hz was explored in Fig. 6. The first measurement number at a particular temperature corresponds to 100 % SoC and the last number to 0 % SoC. An average of 30 EIS measurements were performed during discharge. The effects of SoC on estimates are clearly visible for the two extremes of temperature at 10 °C and 55 °C but is also observable to a much lesser degree at the other temperatures. This is characterised by a diagonal slope on the estimate compared to the actual temperature (Fig. 6a). Interestingly, the trend for high (>30 °C) and low temperatures (<30 °C) behave oppositely to each other with the imaginary part of impedance for temperatures >30 °C increasing as the SoC decreased and the imaginary part of impedance decreasing for temperatures <30 °C, as the SoC decreased. The mid temperature regions of 25 °C – 30 °C remain relatively unchanged over the entire range of SoCs. This is more clearly presented in Fig. 6c where the effect of temperature on SoC dependence is presented via a GOF graph. Here we see that the two extremes of temperature showed the highest correlation to the change in SoC. This correlation decreased as the temperature approached the mid-temperature range of 25 °C – 30 °C. This phenomenon can be attributed to the altered kinetics of the LIB at low and high temperatures, which alters the region where 200 Hz is located on the Nyquist plot (Fig. 6d). At high temperatures, the location where 200 Hz is located shifts further to the left on the impedance spectra, compared to 25 °C, where the effect of SoC becomes more dominant. At low temperatures, the opposite occurred where 200 Hz shifts to the right towards the diffusion-controlled region. Both of these shifts in the location where 200 Hz occurred on the impedance spectra means that the impedance gathered no longer fully characterises the area on the impedance spectra where the impedance from the SEI layer occurred, which is highly temperature dependent and SoC independent. This resulted in greater influence from SoC on the impedance variable. This effect can be seen in the Nyquist plot in Fig. S5 that shows the impedance spectra as a function of SoC. It can be seen that at all SoCs, the point at which 200 Hz occurred does not change indicating its low sensitivity to SoC. However, any deviation from this point would result in an increase in SoC dependence.

### 3.4. Estimation of battery internal temperature

To validate the accuracy of the temperature estimation model, nine separate batteries were tested using random changes in temperature. Each battery received its own calibration prior to testing. The calibration coefficients for each battery are shown in Table 1, where M is the gradient of the line and C is the intercept. The M1 and C1 coefficients, used for 10 °C – 35 °C, vary slightly between each battery, which reflects the similar response of each to changes in temperature. The M2 and C2

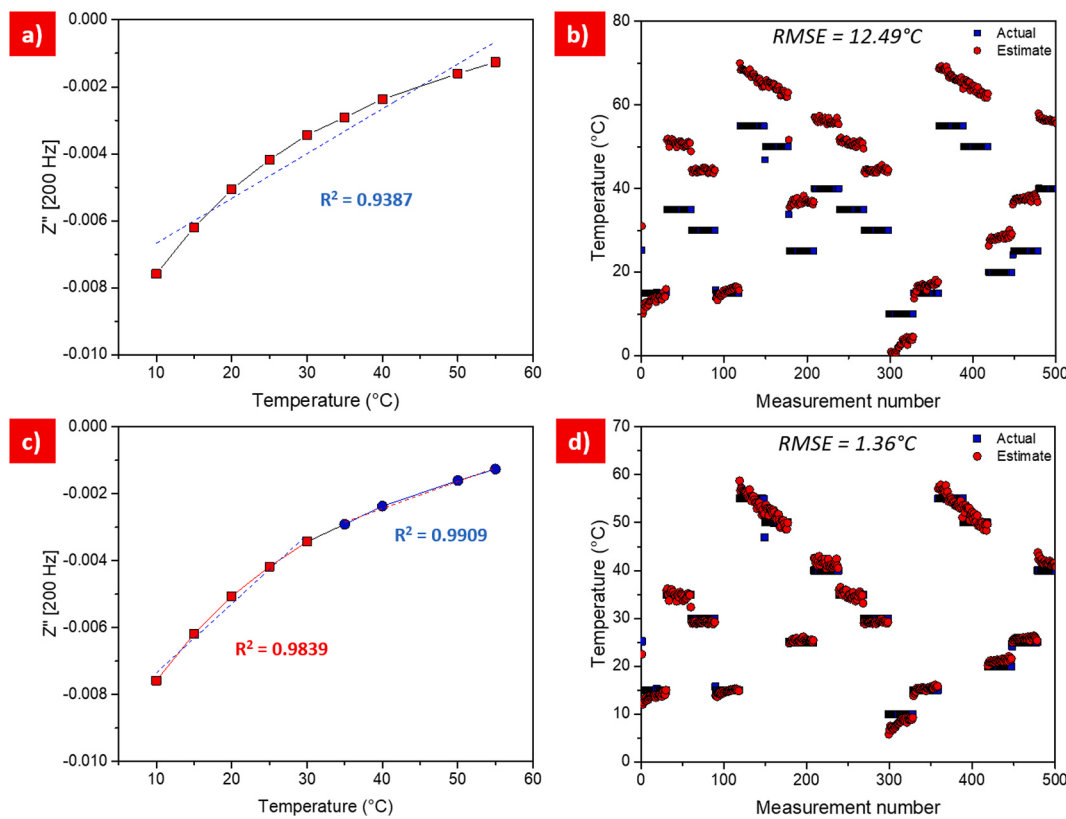


**Fig. 5.** a) One linear fit across all temperatures using the imaginary part of impedance at 200 Hz, b) estimation of temperature using one linear fit, c) two linear fits from 10 °C–35 °C and 35 °C–55 °C using the imaginary part of impedance at 200 Hz, d) estimation of temperature using two linear fits.

coefficients, used for 35 °C – 55 °C, showed more variation. Variability exists between cells in the manufacturing process and so slight differences between each can exist. As a result, cells may exhibit small differences in internal resistance [57]. This demonstrates the need for individual calibration of each battery even though they are of the same chemistry and model. The calibration for each cell is shown in Fig. S6.

Fig. 7 compares the estimated temperature (red circles) to the actual temperature (blue squares) for 2 separate cells with results for the remaining 7 cells shown in the supporting information (Fig. S7). The proposed model is validated over 100 charge/discharge cycles with each change in temperature representing a new cycle. The predicted values showed good agreement with the actual temperature. The maximum RMSE for temperature estimates was 1.61 °C and the minimum was 1.33 °C. From analysis of the 9 batteries, the average RMSE and temperature difference between actual and estimated was 1.41 °C and 1.10 °C respectively. No significant difference in accuracy levels appear across the 9 different cells. Although minimal, the influence of SoH on the temperature estimates can be visually identified by examining the initial estimated temperature data point at each 55 °C temperature phase. Over 100 cycles, this data point migrated to lower temperatures, which is caused by the increase in the batteries internal resistance due to ageing. To account for the influence of SoH on the impedance gathered at 200 Hz, a periodic calibration could be performed in order to correct the impedance-temperature relationship, as outlined in section 2.2. These results prove that the proposed model is effective in characterizing the average internal temperature of Li-ion batteries over extended cycling.

The average temperature RMSE for the 9 tested batteries is presented in Fig. 8a. The RMSE increased as the temperature deviated from the middle temperature region of 25 °C due to greater influence from SoC. An average RMSE of 1.86 °C and 1.80 °C was achieved for 10 °C and 55 °C compared to 0.82 °C at 25 °C. As shown previously in Fig. 6, SoC dependence increased at low and high temperatures, which also

decreased the accuracy of the temperature estimate. The average RMSE across the 9 batteries was determined to be 1.41 °C. Fig. 8b examines the average error distribution of the temperature estimates for the 9 batteries cycled 100 times each. Individual error distribution plots can be seen in Fig. S8. The error ranges from -4 °C to +4 °C with the greatest probability between -1 °C and +1 °C. This low error distribution demonstrates the accuracy and reliability of the model over extended use.

#### 4. Conclusion

Knowing the internal temperature of a LIB at all times is required for its safe and efficient operation. In this paper, we introduce a new approach for online estimation of battery internal temperature using a single frequency online impedance measurement at 200 Hz. By calibrating the change in impedance to the change in temperature, a model was developed that achieved an average RMSE (°C) of 1.41 °C across nine different LIBs. Impedances were gathered online under superimposed DC currents, which to our knowledge is the first time this has been shown for impedance-based temperature estimation. Online acquisition of impedances demonstrates the practicality of bringing impedance measurements from the lab to real world applications. Furthermore, the model was validated over 100 cycles, demonstrating its accuracy and reliability over extended use.

#### CRediT authorship contribution statement

**Kieran Mc Carthy:** Methodology, Validation, Formal analysis, Investigation, Data curation, Writing – original draft, Writing – review & editing, Project administration. **Hemtej Gullapalli:** Resources, Data curation, Writing – review & editing, Supervision, Project administration. **Tadhg Kennedy:** Resources, Writing – review & editing, Supervision, Project administration, Funding acquisition.

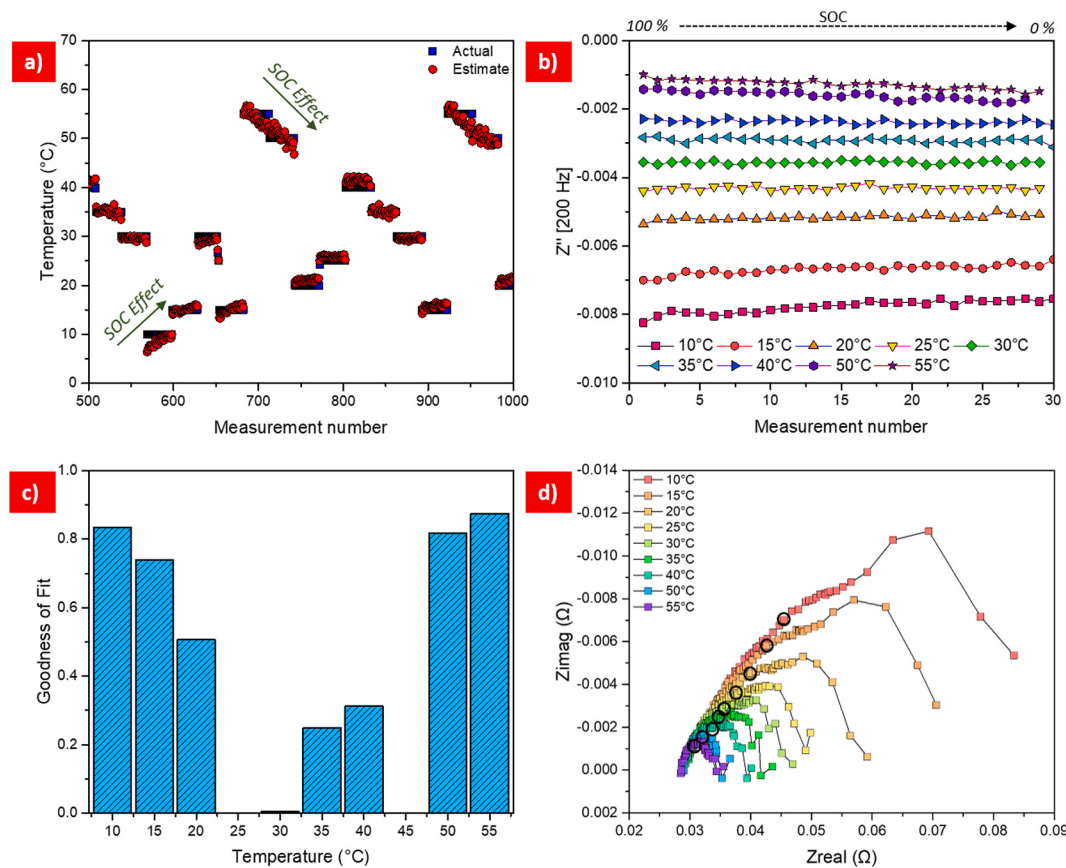


**Fig. 6.** a) Temperature estimation using the imaginary part of impedance at 200 Hz. b) Change in the imaginary part of impedance at 200 Hz at temperatures ranging from 10 °C to 55 °C as a function of SoC. The first measurement number corresponds to 100% SoC and the last to 0% SoC. c) Goodness of fit plot for SoC dependence at various temperatures. A test at 45 °C was not performed. d) Moving location of 200 Hz on the impedance spectra with the change in temperature.

**Table 1**

Model coefficient values, RMSE and average temperate difference for the 9 batteries tested. The M coefficient is the gradient of the line and the C coefficient is the intercept.

Battery I.D.	M1 [10–35 °C]	C1 [10–35 °C]	M2 [35–55 °C]	C2 [35–55 °C]	RMSE	Avg. Temp Diff
1	0.00020	0.00940	0.00080	0.00570	1.36 °C	1.08 °C
2	0.00018	0.00815	0.00057	0.00430	1.33 °C	1.10 °C
3	0.00019	0.00885	0.00070	0.00520	1.44 °C	1.16 °C
4	0.00018	0.00860	0.00070	0.00520	1.61 °C	1.29 °C
5	0.00019	0.00865	0.00070	0.00500	1.41 °C	1.16 °C
6	0.00020	0.00940	0.00070	0.00525	1.48 °C	1.19 °C
7	0.00019	0.00860	0.00060	0.00465	1.33 °C	1.08 °C
8	0.00020	0.00920	0.00070	0.00500	1.34 °C	1.05 °C
9	0.00019	0.0085	0.00060	0.00455	1.42 °C	1.10 °C

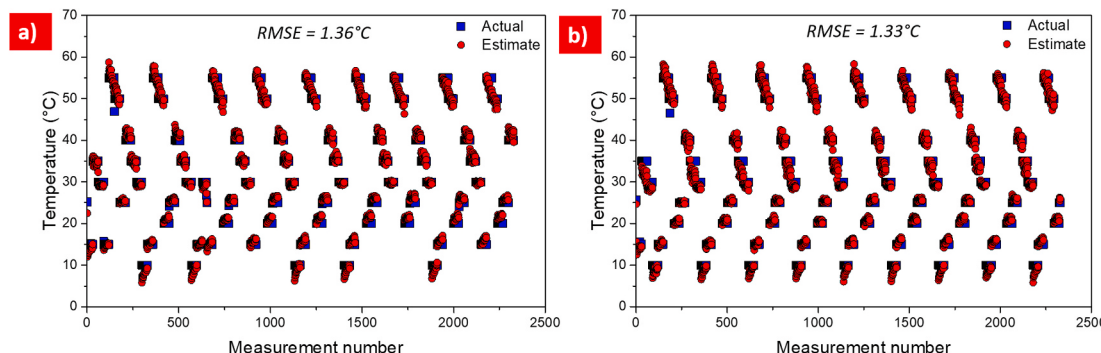


**Fig. 7.** Temperature estimation for two individual cells using the imaginary part of impedance at 200 Hz. A calibration step was performed on each battery prior to cycling.

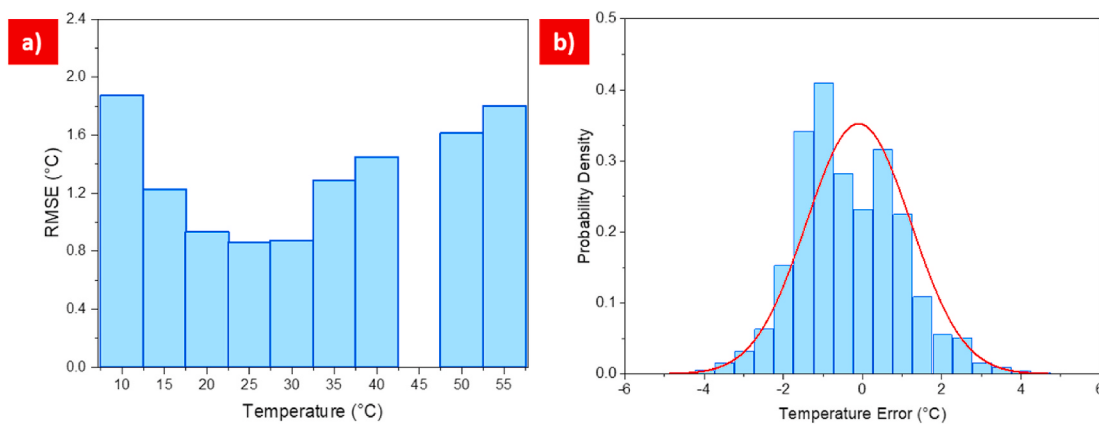


**Fig. 8.** a) Average RMSE as a function of temperature for the 9 batteries. b) Average error distribution of temperature estimates for the 9 batteries.

### Declaration of competing interest

The authors declare that they have no known competing financial interests or personal relationships that could have appeared to influence the work reported in this paper.

### Acknowledgements

This work was made possible by joint financial support from the Irish Research Council (IRC) and Analog Devices International (ADI), under the IRC Enterprise Award Scheme (contract no. EPSPG/2017/377). T.K. acknowledges support from the Sustainable Energy Authority of Ireland through the Research Development and Demonstration Funding Programme (grant no. 19/RDD/548) and from Enterprise Ireland through the Innovation Partnership Programme (grant no. IP 2019 0910). T.K. further acknowledges support from the SFI Research Centre MaREI (award reference no. 12/RC/2302 P2). All authors acknowledge and thank Prof Kevin M. Ryan of the University of Limerick for his support of the research.

### Appendix A. Supplementary data

Supplementary data to this article can be found online at <https://doi.org/10.1016/j.jpowsour.2021.230786>.

### References

- [1] G. Xia, L. Cao, G. Bi, *J. Power Sources* 367 (2017) 90–105.
- [2] X. Lin, H.E. Perez, J.B. Siegel, A.G. Stefanopoulou, Y. Li, R.D. Anderson, Y. Ding, M.P. Castanier, *IEEE Trans. Control Syst. Technol.* 21 (2012) 1745–1755.
- [3] S. Ma, M. Jiang, P. Tao, C. Song, J. Wu, J. Wang, T. Deng, W. Shang, *Prog. Nat. Sci.: Mater. Int.* 28 (2018) 653–666.
- [4] Z. An, L. Jia, Y. Ding, C. Dang, X. Li, *J. Therm. Sci.* 26 (2017) 391–412.
- [5] H. Liu, Z. Wei, W. He, J. Zhao, *Energy Convers. Manag.* 150 (2017) 304–330.
- [6] S. Santhanagopalan, P. Ramadass, J.Z. Zhang, *J. Power Sources* 194 (2009) 550–557.
- [7] A.A. Pesaran, G.-H. Kim, M. Keyser, in: National Renewable energy lab. (NREL), Golden, CO (United States), 2009.
- [8] X. Lin, A.G. Stefanopoulou, J.B. Siegel, S. Mohan, in: ASME 2014 Dynamic Systems and Control Conference, American Society of Mechanical Engineers Digital Collection, 2014.
- [9] Y. Kim, J.B. Siegel, A.G. Stefanopoulou, in: 2013 American Control Conference, IEEE, 2013, pp. 698–703.
- [10] Y. Kim, S. Mohan, J.B. Siegel, A.G. Stefanopoulou, Y. Ding, *IEEE Trans. Control Syst. Technol.* 22 (2014) 2277–2286.
- [11] X. Lin, H.E. Perez, S. Mohan, J.B. Siegel, A.G. Stefanopoulou, Y. Ding, M.P. Castanier, *J. Power Sources* 257 (2014) 1–11.
- [12] M. Fleckenstein, S. Fischer, O. Bohlen, B. Bäker, *J. Power Sources* 223 (2013) 259–267.
- [13] R. Srinivasan, B.G. Carkhuff, M.H. Butler, A.C. Baisden, *Electrochim. Acta* 56 (2011) 6198–6204.
- [14] R. Srinivasan, *J. Power Sources* 198 (2012) 351–358.
- [15] J.P. Schmidt, S. Arnold, A. Loges, D. Werner, T. Wetzel, E. Ivers-Tiffée, *J. Power Sources* 243 (2013) 110–117.
- [16] H. Beelen, L. Raijmakers, M. Donkers, P. Notten, H. Bergveld, *Appl. Energy* 175 (2016) 128–140.
- [17] J. Zhu, Z. Sun, X. Wei, H. Dai, *J. Power Sources* 274 (2015) 990–1004.
- [18] E. Karden, Using low frequency impedance spectroscopy for characterization, monitoring, and modeling of industrial batteries, Shaker (2002).
- [19] N. Takami, A. Satoh, M. Hara, T. Ohsaki, *J. Electrochem. Soc.* 142 (1995) 371–379.
- [20] R. Srinivasan, B.G. Carkhuff, *J. Power Sources* 241 (2013) 560–566.
- [21] J.P. Schmidt, D. Manka, D. Klotz, E. Ivers-Tiffée, *J. Power Sources* 196 (2011) 8140–8146.
- [22] J.P. Schmidt, T. Chrobak, M. Ender, J. Illig, D. Klotz, E. Ivers-Tiffée, *J. Power Sources* 196 (2011) 5342–5348.
- [23] S. Zhang, K. Xu, T. Jow, *Electrochim. Acta* 49 (2004) 1057–1061.
- [24] L. Raijmakers, D. Danilov, J. Van Lammeren, M. Lammers, P. Notten, *J. Power Sources* 247 (2014) 539–544.
- [25] R.R. Richardson, P.T. Ireland, D.A. Howey, *J. Power Sources* 265 (2014) 254–261.
- [26] P. Suresh, A. Shukla, N. Munichandraiah, *J. Appl. Electrochem.* 32 (2002) 267–273.
- [27] Panasonic, in: Panasonic Newsroom, 2019.
- [28] A. Devices, in: Analog Devices Circuit Note, 2019.
- [29] D. Andre, M. Meiler, K. Steiner, C. Wimmer, T. Soczka-Guth, D. Sauer, *J. Power Sources* 196 (2011) 5334–5341.
- [30] A. Barré, B. Deguilhem, S. Grolleau, M. Gérard, F. Suard, D. Riu, *J. Power Sources* 241 (2013) 680–689.
- [31] V. Choudhari, A. Dhoble, T. Sathe, *J. Energy Storage* 32 (2020) 101729.
- [32] S. Zhang, K. Xu, T. Jow, *J. Power Sources* 115 (2003) 137–140.
- [33] B.V. Ratnakumar, M.C. Smart, S. Surampudi, *J. Power Sources* 97–98 (2001) 137–139.
- [34] A. Senyshyn, M.J. Mühlbauer, O. Dolotko, H. Ehrenberg, *J. Power Sources* 282 (2015) 235–240.
- [35] S.S. Zhang, K. Xu, T.R. Jow, *Electrochim. Acta* 48 (2002) 241–246.
- [36] S.S. Zhang, K. Xu, T.R. Jow, *J. Power Sources* 160 (2006) 1403–1409.
- [37] S.S. Zhang, K. Xu, T.R. Jow, *Electrochim. Acta* 49 (2004) 1057–1061.
- [38] T.R. Jow, S.A. Delp, J.L. Allen, J.-P. Jones, M.C. Smart, *J. Electrochem. Soc.* 165 (2018) A361–A367.
- [39] P. Suresh, A.K. Shukla, N. Munichandraiah, *J. Appl. Electrochem.* 32 (2002) 267–273.
- [40] S. Fletcher, *J. Electrochem. Soc.* 141 (1994) 1823–1826.
- [41] M.D. Murbach, D.T. Schwartz, *J. Electrochem. Soc.* 164 (2017) E3311–E3320.
- [42] B.G. Carkhuff, P.A. Demirev, R. Srinivasan, *IEEE Trans. Ind. Electron.* 65 (2018) 6497–6504.
- [43] S. Rodrigues, N. Munichandraiah, A. Shukla, *J. Solid State Electrochem.* 3 (1999) 397–405.
- [44] S. Lee, J. Kim, J. Lee, B.H. Cho, *J. Power Sources* 185 (2008) 1367–1373.
- [45] A. Cuadras, O. Kanoun, in: 2009 6th International Multi-Conference on Systems, Signals and Devices, IEEE, 2009, pp. 1–5.
- [46] A. Zenati, P. Desprez, H. Razik, in: IECON 2010-36th Annual Conference on IEEE Industrial Electronics Society, IEEE, 2010, pp. 1773–1778.
- [47] M. Galeotti, L. Cinà, C. Giannamico, S. Cordiner, A. Di Carlo, *Energy* 89 (2015) 678–686.
- [48] X. Zhou, Z. Pan, X. Han, L. Lu, M. Ouyang, *J. Power Sources* 417 (2019) 188–192.
- [49] A. Eddahech, O. Briat, N. Bertrand, J.-Y. Deletage, J.-M. Vinassa, *Int. J. Electr. Power Energy Syst.* 42 (2012) 487–494.
- [50] C.T. Love, K. Swider-Lyons, *Electrochim. Solid State Lett.* 15 (2012) A53.
- [51] X. Wang, X. Wei, H. Dai, *J. Energy Storage* 21 (2019) 618–631.
- [52] L. Chen, Z. Lü, W. Lin, J. Li, H. Pan, *Measurement* 116 (2018) 586–595.
- [53] U. Tröltzsch, O. Kanoun, H.-R. Tränkler, *Electrochim. Acta* 51 (2006) 1664–1672.
- [54] C.R. Birk, M.R. Roberts, E. McTurk, P.G. Bruce, D.A. Howey, *J. Power Sources* 341 (2017) 373–386.

- [55] N. Ogihara, Y. Itou, T. Sasaki, Y. Takeuchi, *J. Phys. Chem. C* 119 (2015) 4612–4619.
- [56] M.S. Hosen, R. Gopalakrishnan, T. Kalogiannis, J. Jaguemont, J. Van Mierlo, M. Berecibar, *World Electr. Veh. J.* 12 (2021) 77.
- [57] D. Shin, M. Poncino, E. Macii, N. Chang, in: International Symposium on Low Power Electronics and Design (ISLPED), 2013, pp. 94–99.